Van der Waals heterostructure Pt₂HgSe₃/CrI₃ for topological valleytronics

Zheng Liu,[1,*] Yulei Han [1,2,*] Yafei Ren,[3,*] Qian Niu,[3] and Zhenhua Qiao [1,†]

[1]*ICQD, Hefei National Laboratory for Physical Sciences at Microscale, CAS Key Laboratory of Strongly-Coupled Quantum Matter Physics, and Department of Physics, University of Science and Technology of China, Hefei, Anhui 230026, China*
[2]*Department of Physics, Fuzhou University, Fuzhou, Fujian 350108, China*
[3]*Department of Physics, The University of Texas at Austin, Austin, Texas 78712, USA*

We identify a valley-polarized Chern insulator in a van der Waals heterostructure, monolayer Pt₂HgSe₃/monolayer CrI₃, for potential applications with interplay between electric, magnetic, optical, and mechanical effects. The interlayer proximity magnetic coupling nearly closes the band gap of monolayer Pt₂HgSe₃, and the strong intralayer spin-orbit coupling further lifts the valley degeneracy by over 100 meV, leading to positive and negative band gaps at opposite valleys. In the valley with negative gap, the interfacial Rashba spin-orbit coupling opens a topological band gap of 17.8 meV, which is enlarged to 30.8 meV by adding a hexagonal boron nitride (*h*-BN) layer. We find large orbital magnetization in the Pt₂HgSe₃ layer that is much larger than spin, which can induce a measurable optical Kerr effect. The valley polarization and Chern number are coupled to the magnetic order of the nearest-neighbor CrI₃ layer, which is switchable by electric, magnetic, and mechanical means in experiments. The presence of *h*-BN protects the topological phase, allowing the construction of superlattices with valley, spin, and layer degrees of freedom.

Introduction. The inequivalent electronic band extrema of graphene at K and K' inspired the development of valleytronics [1], which encodes information in the valley binary and focuses on its generation, manipulation, and detection [2,3]. With breaking inversion symmetry, the valley contrasting orbital magnetic moment and valley Hall effect have been demonstrated and materialized in transition metal dichalcogenide (TMD) monolayers [4,5]. In these materials, the generation and manipulation of valley polarization have been realized by optical or magnetic fields [6–19]. Despite such successes in experiments, these methods are difficult to scale, which limits their potential future application. Electrical control of the valley degree of freedom, which is scalable and more compatible with current semiconductor technology, is thus still highly desired.

The electrical generation of valley polarization can be achieved when the valley degeneracy is lifted by breaking the time reversal symmetry [12–18], which can be achieved by applying a magnetic field or proximity coupling to magnetic substrates [20–33]. By using a bulk magnetic substrate, valley splitting in TMD layers is observed, but the magnitude is limited to several meV [23,24]. Moreover, to manipulate the valley polarization one needs to switch the magnetization of the bulk substrate, which is, however, very challenging to achieve by electrical means. In contrast, recent developments in two-dimensional van der Waals (vdW) magnets [34–39] open up such a possibility [31–33,37–40]. The CrI₃ monolayer has a very strong intralayer ferromagnetic order with out-of-plane magnetization. The ground state of bilayer CrI₃ has intralayer ferromagnetic and interlayer antiferromagnetic

orders [35,41–43]. Switching of magnetization of CrI₃ few layers have been achieved in experiments by applying electric or magnetic fields or external strain [35,36], which allows the construction of a valley-field-effect transistor and other devices with interplay between electric, magnetic, optical, and mechanical effects.

A proper material candidate showing large valley polarization induced by CrI₃ is, however, still lacking despite several attempts. In a TMD/CrI₃ heterostructure, the valley splitting is limited to a few meV due to the band alignment being faulty [32,33,40]. In addition, the energy bands of CrI₃ lie inside the band gap of TMD materials. This alters the intrinsic band structure of TMD layers and can even close its band gap [40]. In the stanene/CrI₃ heterostructure [44], although the valley splitting energy bands are realized, they show strong overlapping with the substrate's bands.

In this Letter, we propose an ideal material system, Pt₂HgSe₃/CrI₃, showing large valley splitting and a nonzero Chern number. In the absence of spin-orbit coupling (SOC), the interlayer magnetic proximity effect nearly closes the band gap of Pt₂HgSe₃. The strong intralayer SOC induces energy gaps with opposite signs in the K and K' valleys, leading to large valley splitting over 100 meV. The interfacial Rashba SOC further opens a gap of 17.8 meV with a nonzero Chern number in the negatively gapped valley. In the Pt₂HgSe₃ layer, we identify a large orbital magnetic moment that is larger than that from the spin, which can induce an orbital-magnetization-based optical Kerr effect. We find that the valley polarization and Chern number are coupled to the magnetism of the nearest-neighbor CrI₃ and are robust against the increasing of the CrI₃ thickness. In the presence of a hexagonal boron nitride (*h*-BN) layer, we find that the topological band gap can be enlarged to 30.8 meV, whereas the valley splitting remains large. The protection provided by the *h*-BN layer
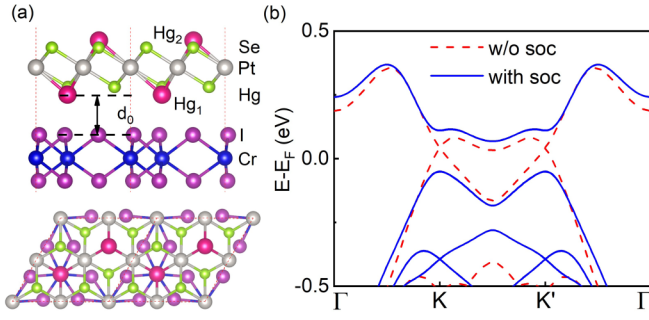
FIG. 1. (a) The structure of the Pt_2HgSe_3/CrI_3 heterostructure. The pink, silver, green, blue, and purple balls are for Hg, Pt, Se, Cr, and I atoms, respectively. d_0 represents the optimized vdW gap, and the two buckled Hg sites are denoted as Hg_1 and Hg_2. (b) Band structure of monolayer Pt_2HgSe_3 without and with SOC.

further allows the construction of superlattices with valley, spin, and layer degrees of freedom.

Atomic structures. We focus on the Pt_2HgSe_3-based heterostructure as displayed in Fig. 1(a). The bulk Pt_2HgSe_3 is experimentally demonstrated as a dual topological semimetal [45], which can be exfoliated down to a few layers that are expected to be stable under ambient conditions [46]. The Hg atoms, which contribute dominantly to the energy bands near the Fermi energy, form a buckled honeycomb lattice. The electronic structure of a freestanding Pt_2HgSe_3 monolayer is plotted in Fig. 1(b). In the absence of spin-orbit coupling, linear dispersion exists around the K and K' points, shown by dashed lines. When the spin-orbit coupling is further included, a large band gap opens, as plotted by solid lines, which indicates that Pt_2HgSe_3 can be considered a Kane-Mele-type topological insulator [47–49].

By placing Pt_2HgSe_3 on CrI_3, the magnetism can be induced by the proximity effect, which depends strongly on the atomic wave function overlap. Thus, the two sublattices of Hg atoms are expected to experience different exchange fields. We denote the sublattice of Hg near CrI_3 as Hg_1, and the other sublattice is denoted Hg_2. In our calculation, we adopt a 1×1 Pt_2HgSe_3/CrI_3 unit cell with a lattice mismatch of 4.5%. As we mainly focus on the band structure evolutions of Pt_2HgSe_3, we stretch the CrI_3 monolayer for the simulation of Pt_2HgSe_3/CrI_3. We find that the main properties of the CrI_3 monolayer are not substantially changed after stretching [50].

Effective model of valley splitting. Before demonstrating detailed first-principles calculation results, an analysis based on an effective model helps to illustrate the underlying physics clearly. The electronic structure of Pt_2HgSe_3 can be described by the Kane-Mele model of $H_0 + H_{ISO}$, where $H_0 = \hbar v_F(\tau_z \sigma_x k_x + \sigma_y k_y)s_0$ describes its Dirac dispersion in the absence of spin-orbit coupling, where the Fermi velocity term $\hbar v_F = 1.97\,\text{eV/Å}$ and $H_{ISO} = \lambda \tau_z \sigma_z s_z$ is the intrinsic spin-orbit coupling with $\lambda = 81.2\,\text{meV}$. s and σ are Pauli matrices for the spin and sublattice, respectively, and $\tau_z = 1$ (-1) describes valley index K (K').

The presence of a magnetic substrate breaks both inversion ($\mathcal{P}$) and time reversal ($\mathcal{T}$) symmetries and leads to inequivalent exchange fields $m_{1,2}$ on Hg_1 and Hg_2, which can be described by $H_{EX} = m_+\sigma_0 s_z + m_-\sigma_z s_z$, where $m_\pm = (m_1 \pm$
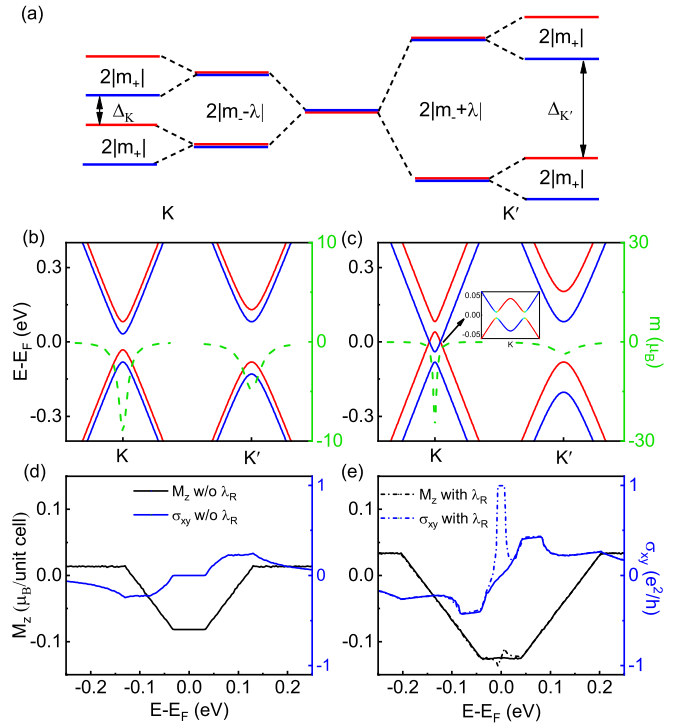
FIG. 2. (a) The influence of symmetric and antisymmetric exchange fields on the band gaps in the K and K' valleys. The band structure and orbital magnetic moment around the K and K' valleys for (b) $m_1 = 0.6\lambda$ and (c) $m_1 = 1.5\lambda$. The inset of (c) shows the band near the Fermi energy with the inclusion of small Rashba spin-orbit coupling. Red (blue) denotes the spin-up (spin-down) state. (d) and (e) The corresponding orbital magnetization in a unit cell and anomalous Hall conductance. The solid (dotted) line represents the system without (with) Rashba spin-orbit coupling.

$m_2)/2$ stand for the symmetric and antisymmetric parts of the inequivalent exchange fields. The symmetric part is the Zeeman field splitting of the spin degree of freedom. The antisymmetric part together with H_{ISO} gives rise to a mass term, $(m_- + \lambda \tau_z)\sigma_z s_z$, where s_z indicates the spin-contrast sign of mass leading to, in contrast to TMD, a vanishing valley Chern number. The presence of τ_z leads to valley-dependent band gaps, as illustrated in Fig. 2(a). In this case, the spin-up and -down bands are still degenerate since the $\mathcal{PT}$ symmetry remains, which also guarantees a vanishing magnetization and anomalous Hall response. When the symmetric part m_+ is further included, $\mathcal{PT}$ symmetry is broken, which lifts the spin degeneracy and valley-dependent band gaps. Nonzero orbital magnetization and anomalous Hall responses can also appear.

By fitting to the first-principles result, we find that $|m_1| \gg |m_2|$ since the Hg_2 atoms are farther away from the magnetic substrate. We thus set $m_2 = 0$ for simplicity. With a moderate exchange field $|m_1| < \lambda$, we plot the energy bands in Fig. 2(b) by solid lines where one can find spin-valley splitting. These valley-splitting energy bands exhibit large orbital magnetic moment, as shown by green dashed lines, where the magnetic moment of the valence band maximum can reach about $9.0\mu_B$ ($4.9\mu_B$) around the K (K') point for $m_1 = 0.6\lambda$. When the Fermi energy lies inside the band gap, finite orbital magnetization appears on the order of $0.1\mu_B$ per unit cell, as shown
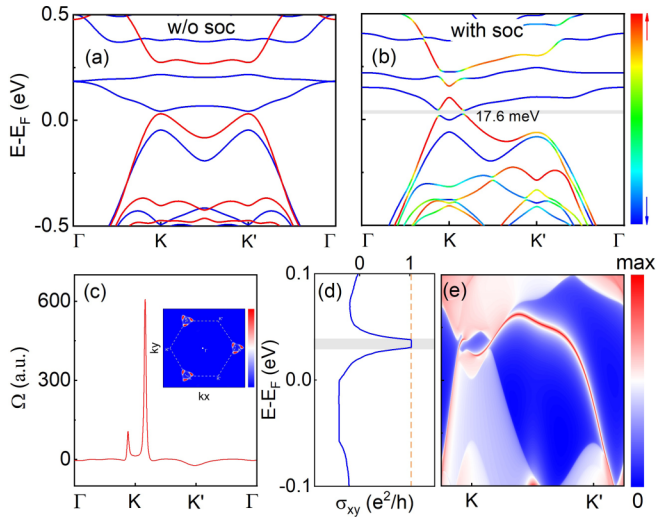
FIG. 3. (a) and (b) Band structure of Pt_2HgSe_3/CrI_3 (a) without and (b) with SOC. In (a), red (blue) represents the spin-up (spin-down) state. In (b), $\Delta_K = -105.5$ meV, and $\Delta_{K'} = 167.1$ meV, with valley splitting $\Delta = (\Delta_{K'} - \Delta_K)/2 = 136.3$ meV. The gap with a negative sign indicates the presence of band inversion. (c) The Berry curvature along the high-symmetry lines. The inset shows the Berry curvature in the first Brillouin zone. (d) The Fermi energy dependence of the anomalous Hall conductivity. (e) The local density of states of a semi-infinite zigzag ribbon of the Pt_2HgSe_3/CrI_3 heterostructure.

in Fig. 2(d), which is larger than the spin magnetization of Hg atoms. The presence of orbital magnetization suggests the presence of the anomalous Hall effect, Kerr effect, etc. [51–55].

The valley splitting gradually increases as the inequivalent exchange field increases, as plotted in Fig. 2(c). Meanwhile, the larger m_1 makes the effective mass smaller in valley K, resulting in a larger orbital magnetic moment that is about $25.2\mu_B$ for $m_1 = 1.5\lambda$. The corresponding orbital magnetization and anomalous Hall effect are also stronger, as illustrated in Fig. 2(e). More importantly, when $|m_+| > |m_- - \lambda|$, the band inversion appears between two bands with opposite spins. In this case, the interfacial Rashba spin-orbit coupling $H_R = \lambda_R(\tau_z\sigma_x s_y - \sigma_y s_x)$ plays an essential role, which reopens a band gap in the K valley, as shown in the inset, which harbors the quantum anomalous Hall effect (QAHE) with a Chern number of $\mathcal{C} = 1$. Such a topological property is demonstrated by the quantized Hall conductance and linear dependence of magnetization on the chemical potential inside the band gap.

Fully valley-polarized QAHE in Pt_2HgSe_3/CrI_3. The first-principles calculations agree well with our theoretical analysis. The valley-polarized QAHE can really be formed in the Pt_2HgSe_3/CrI_3 heterostructure, as displayed in Figs. 3(a) and 3(b), where we plot the electronic structures without and with spin-orbit coupling, respectively. In the absence of spin-orbit coupling, the magnetic proximity effect leads to a large spin splitting, while the valley degeneracy is preserved. The nearly flat band above the Fermi level arises from the hybridization with CrI_3 bands but does not affect the physics described above [50]. When the spin-orbit coupling is further

included, a strong valley splitting of 136.3 meV is observed, as shown in Fig. 2(b), where a band inversion appears in the K valley with a band gap of 17.6 meV. The color of the spin projection agrees with our above model, indicating that the band gap is opened by the Rashba spin-orbit coupling and is topologically nontrivial.

To confirm the band topology, we calculate the Berry curvature by using maximally localized Wannier functions [56]. We find that the Berry curvature shows sharp positive peaks in the K valley, whereas it becomes vanishingly small in the K' valley, as shown in Fig. 3(c). By integrating the Berry curvature around the K and K' valleys, we find that the valley-dependent Chern numbers are $\mathcal{C}_K = 1$ and $\mathcal{C}_{K'} = 0$. Thus, the corresponding total Chern number is $\mathcal{C} = \mathcal{C}_K + \mathcal{C}_{K'} = 1$, and the valley Chern number is $\mathcal{C}_V = \mathcal{C}_K - \mathcal{C}_{K'} = 1$, indicating the presence of a fully valley-polarized QAHE. The energy dependence of the anomalous Hall conductance is plotted in Fig. 3(d), which shows a quantized value of e^2/h in the energy gap. Such a topological phase is further confirmed by studying the topological edge states [57,58]. As shown in Fig. 2(e), we find two gapless edge modes with positive group velocity in the K valley connecting the valence and conduction bands, whereas one edge state appears in the K' valley with opposite velocity. The number difference of the left- and right-moving edge states in different valleys agrees with the Chern number as well as the valley Chern number.

Besides the band topology, the first-principles calculations can provide further details about the magnetism in the heterostructure. The proximity effect leads to different magnetic moments at two Hg atoms, i.e., the local magnetic moment is $0.015\mu_B$ in Hg_1, which is parallel to the CrI_3, whereas a magnetic moment of $-0.017\mu_B$ is induced in Hg_2 with opposite sign. It is noteworthy that the net spin magnetic moment is three orders of magnitude smaller than that from the orbital contribution, indicating that the large orbital magnetic moment plays a crucial role in the Pt_2HgSe_3-based system. In addition, the local magnetic moment of Cr is also increased by $0.5\mu_B$ compared to that in the pristine CrI_3 monolayer ($3.0\mu_B/Cr$) [59]. As a result, the Heisenberg exchange constant increases to $J_0 = -5.23$ meV, which corresponds to a Curie temperature of 91 K [50]. Therefore, the magnetism can be enhanced in the heterostructure, benefiting the realization of high-temperature valley-polarized QAHE.

h-BN/Pt_2HgSe_3/CrI_3 as a building block. To study the scalability of the heterostructure, we investigate the influence of h-BN on the topological phase since h-BN is widely used in experiments as a dielectric layer, which is atomically flat, is stable in air and at high temperature, and can protect the vdW layers from contamination and degradation [60,61]. By considering the trilayer system illustrated in Fig. 4(a), we plot the energy bands with spin-orbit coupling in Fig. 4(b), where the large valley splitting remains and the topological band gap is nearly doubled to 30.8 meV, larger than the one without h-BN. The increase of the topological band gap is considered the result of sublattice potential δ changes [50]. The effect of sublattice potential changes was also reported in a recent work [62] in which h-BN was used to tune the band gap of bilayer Pt_2HgSe_3. As the electrical control of the magnetism of CrI_3 is experimentally found in its bilayers, we also studied the Pt_2HgSe_3/CrI_3 bilayer structure and found similar results
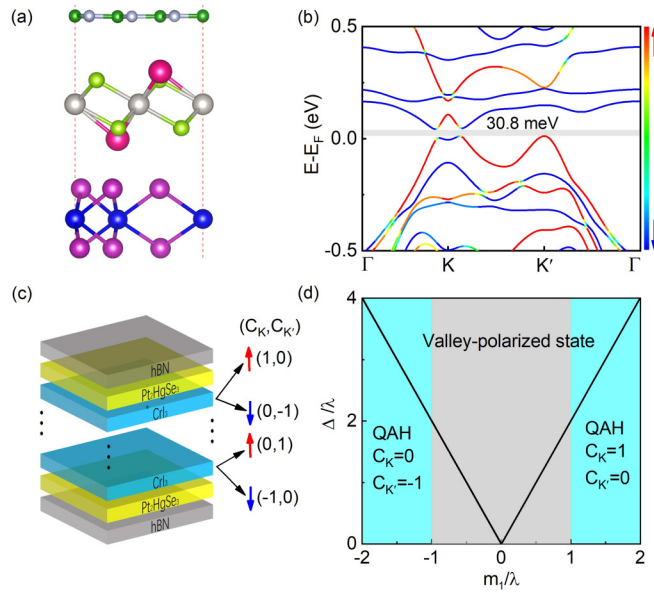
FIG. 4. (a) Lattice and (b) electronic structures of h-BN/Pt$_2$HgSe$_3$/CrI$_3$ with SOC. Here, $\Delta_K = -113.4$ meV, and $\Delta_{K'} = 137.4$ meV, with valley splitting $\Delta = 125.4$ meV. The gap with a negative sign indicates the presence of band inversion. (c) vdW superlattice consisting of an h-BN/Pt$_2$HgSe$_3$/CrI$_3$ multilayer as building blocks to realize abundant topological phase coupled spin, valley, and layer degrees of freedom with Chern numbers. (d) Valley splitting Δ and phase diagram as a function of m_1/λ.

[50], which greatly improves the application potentials of the vdW layers studied here.

The enhanced valley-polarized QAHE with the encapsulated h-BN layer and its robustness with increasing CrI$_3$ thickness not only make the QAHE achievable at higher temperature but also make h-BN/Pt$_2$HgSe$_3$/CrI$_3$ a perfect building block to realize multifunctional electronics. By reversing the stacking order from h-BN/Pt$_2$HgSe$_3$/CrI$_3$ to CrI$_3$/Pt$_2$HgSe$_3$/h-BN, one can change the valley polarization without changing the Chern number. Moreover, with the stacking order fixed, the valley polarization and Chern number can be simultaneously reversed by reversing the magnetization. Therefore, by changing the stacking orders and magnetization directions, one can control the spin, valley, and layer degrees of freedom with the Chern number in a superlattice structure, as illustrated in Fig. 4(c). Rich structures with different functionalities in the spin- and valleytronics are expected.

In Fig. 4(d), we plot the phase diagram and valley splitting as a function of m_1/λ. We can see that the valley-polarized quantum anomalous Hall effect can be achieved when $|m_1/\lambda_0| > 1$, and valley splitting can still be there as long as m_1/λ is not zero. Therefore, the valley-polarized QAHE is expected in other material candidates in the Pt$_2$HgSe$_3$ family [48,63,64] by suitably choosing the magnetic substrates.

Summary. We proposed the vdW heterostructure Pt$_2$HgSe$_3$/CrI$_3$ as an ideal material system to realize topological valleytronics with the interplay between electric, magnetic, optical, and mechanical effects. The imbalanced proximity exchanged field and the intrinsic strong SOC of Pt$_2$HgSe$_3$ lead to a large valley splitting over 100 meV. In the valley with band inversion, the interfacial Rashba SOC leads to a Chern insulator with a band gap of 17.8 meV, which can be enlarged to 30.8 meV in the presence of h-BN. The valley-encoded dissipationless edge states benefit the realization of low-energy-consumption topological devices. Large orbital magnetization and negligible spin magnetization were identified in Pt$_2$HgSe$_3$, which can lead to an orbital effect dominated optical Kerr effect and anomalous Hall effect. This not only benefits the electrical and optical detection of the valley index but also provides an opportunity to switch the magnetism and valley polarization via electric current at finite doping.

The valley polarization and Chern number were coupled to the magnetism of the nearest-neighbor CrI$_3$ and were robust against the increasing of the CrI$_3$ thickness. The experimentally demonstrated switching of the magnetism in CrI$_3$ few layers by electric, magnetic, or mechanical means opens up the possibility to realize valleytronic devices controlled by these methods. Particularly, the electrical switching of the magnetism lays the foundation of its application in electrically controllable valleytronics, e.g., the valley-field-effect transistor, which can combine the advantage of nontrivial band topology and dissipationless kink states at the domain walls. Moreover, the robustness of the topological phase in the presence of an h-BN layer opens up the possibility to construct superlattices with valley, spin, and layer degrees of freedom.

Besides CrI$_3$, we found that other magnetic insulators, e.g., MnI$_2$, can also be used as substrate materials to realize the valley-polarized QAHE in Pt$_2$HgSe$_3$-based vdW heterostructures [50]. Considering the continuously growing family of vdW layers with different functionalities, e.g., magnetism, large-gap dielectric materials, and large-gap $\mathbb{Z}_2$ topological insulators in the jacutingaite family [48,63,64], our results suggest a way to search for material candidates with novel physics and application potentials in topological valleytronics.

[1] A. Rycerz, J. Tworzydlo, and C. W. J. Beenakker, Nat. Phys. **3**, 172 (2007).

[2] J. R. Schaibley, H. Yu, G. Clark, P. Rivera, J. S. Ross, K. L. Seyler, W. Yao, and X. Xu, Nat. Rev. Mater. **1**, 16055 (2016).

[3] S. A. Vitale, D. Nezich, J. O. Varghese, P. Kim, N. Gedik, P. Jarillo-Herrero, D. Xiao, and M. Rothschild, Small **14**, 1801483 (2018).

[4] D. Xiao, W. Yao, and Q. Niu, Phys. Rev. Lett. **99**, 236809 (2007).

[5] D. Xiao, G.-B. Liu, W. Feng, X. Xu, and W. Yao, Phys. Rev. Lett. **108**, 196802 (2012).

[6] G. Liu, D. Xiao, Y. Yao, X. Xu, and W. Yao, Chem. Soc. Rev. **44**, 2643 (2015).

[7] K. F. Mak, K. He, J. Shan, and T. F. Heinz, Nat. Nanotechnol. **7**, 494 (2012).

[8] T. Cao, G. Wang, W. Han, H. Ye, C. Zhu, J. Shi, Q. Niu, P. Tan, E. Wang, B. Liu, and J. Feng, Nat. Commun. **3**, 887 (2012).

[9] H. Zeng, J. Dai, W. Yao, D. Xiao, and X. Cui, Nat. Nanotechnol. **7**, 490 (2012).

[10] A. M. Jones, H. Yu, N. J. Ghimire, S. Wu, G. Aivazian, J. S. Ross, B. Zhao, J. Yan, D. G. Mandrus, D. Xiao, W. Yao, and X Xu, Nat. Nanotechnol. **8**, 634 (2013).

[11] K. F. Mak, K. L. McGill, J. Park, and P. L. McEuen, Science **344**, 1489 (2014).

[12] J. Kim, X. Hong, C. Jin, S. Shi, C. S. Chang, M. Chiu, L. Li, and F. Wang, Science **346**, 1205 (2014).

[13] A. Srivastava, M. Sidler, A. V. Allain, D. S. Lembke, A. Kis, and A. Imamoglu, Nat. Phys. **11**, 141 (2015).

[14] H. Rostami and R. Asgari, Phys. Rev. B **91**, 075433 (2015).

[15] G. Aivazian, Z Gong, A. M. Jones, R. Chu, J. Yan, D. G. Mandrus, C. Zhang, D. Cobden, W. Yao, and X. Xu, Nat. Phys. **11**, 148 (2015).

[16] A. V. Stier, K. M. McCreary, B. T. Jonker, J. Kono, and S. A. Crooker, Nat. Commun. **7**, 10643 (2016).

[17] D. MacNeill, C. Heikes, K. F. Mak, Z. Anderson, A. Kormanyos, V. Zolyomi, J. Park, and D. C. Ralph, Phys. Rev. Lett. **114**, 037401 (2015).

[18] Y. Li, J. Ludwig, T. Low, A. Chernikov, X. Cui, G. Arefe, Y. D. Kim, A. M. van der Zande, A. Rigosi, H. M. Hill, S. H. Kim, J. Hone, Z. Li, D. Smirnov, and T. F. Heinz, Phys. Rev. Lett. **113**, 266804 (2014).

[19] Z.-M. Yu, S. Guan, X.-L. Sheng, W. Gao, and S. A. Yang, Phys. Rev. Lett. **124**, 037701 (2020).

[20] J. Qi, X. Li, Q. Niu, and J. Feng, Phys. Rev. B **92**, 121403(R) (2015).

[21] Q. Zhang, S. A. Yang, W. Mi, Y. Cheng, and U. Schwingenschlogl, Adv. Mater. **28**, 959 (2016).

[22] X. Liang, L. Deng, F. Huang, T. Tang, C. Wang, Y. Zhu, J. Qin, Y. Zhang, B. Peng, and L. Bi, Nanoscale **9**, 9502 (2017).

[23] C. Zhao, T. Norden, P. Zhang, P. Zhao, Y. Cheng, F. Sun, J. P. Parry, P. Taheri, J. Wang, Y. Yang, T. Scrace, K. Kang, S. Yang, G. Miao, R. Sabirianov, G. Kioseoglou, W. Huang, A. Petrou, and H. Zeng, Nat. Nanotechnol. **12**, 757 (2017).

[24] T. Norden, C. Zhao, P. Zhang, R. Sabirianov, A. Petrou, and H. Zeng, Nat. Commun. **10**, 4163 (2019).

[25] L. Xu, M. Yang, L. Shen, J. Zhou, T. Zhu, and Y. P. Feng, Phys. Rev. B **97**, 041405(R) (2018).

[26] X. Xue, X. Wang, and W. Mi, J. Phys. D **52**, 115303 (2019).

[27] B. Zhou, Z. Li, J. Wang, X. Niu, and C. Luan, Nanoscale **11**, 13567 (2019).

[28] Y. Song, X. Wang, and W. Mi, Adv. Electron. Mater. **3**, 1700245 (2017).

[29] G. Yang, J. Li, H. Ma, Y. Yang, C. Li, X. Mao, and F. Yin, Phys. Rev. B **98**, 235419 (2018).

[30] Y. Song, Q. Zhang, W. Mi, and X. Wang, Phys. Chem. Chem. Phys **18**, 15039 (2016).

[31] C. Ke, Y. Wu, W. Yang, Z. Wu, C. Zhang, X. Li, and J. Kang, Phys. Rev. B **100**, 195435 (2019).

[32] K. L. Seyler, D. Zhong, B. Huang, X. Linpeng, N. P. Wilson, T. Taniguchi, K. Watanabe, W. Yao, D. Xiao, M. A. McGuire, K. C. Fu, and X. Xu, Nano Lett. **18**, 3823 (2018).

[33] K. Zollner, P. E. Faria Junior, and J. Fabian, Phys. Rev. B **100**, 085128 (2019).

[34] D. L. Duong, S. J. Yun, and Y. H. Lee, ACS Nano **11**, 11803 (2017).

[35] S. Jiang, J. Shan, and K. F. Mak, Nat. Mater. **17**, 406 (2018).

[36] K. F. Mak, J. Shan, and D. C. Ralph, Nat. Rev. Phys. **1**, 646 (2019).

[37] I. Žutić, A. Matos-Abiague, B. Scharf, H. Dery, and K. Belashchenko, Mater. Today **22**, 85 (2019).

[38] M. Wang, C. Huang, C. Cheung, C. Chen, S. G. Tan, T. Huang, Y. Zhao, Y. Zhao, G. Wu, Y. Feng, H. Wu, and C. Chang, Ann. Phys. (Berlin, Ger.) **532**, 1900452 (2020).

[39] B. Huang, M. A. McGuire, A. F. May, D. Xiao, P. Jarillo-Herrero, and X. Xu, Nat. Mater. **19**, 1276 (2020).

[40] H. Zhang, W. Yang, Y. Ning, and X. Xu, Phys. Rev. B **101**, 205404 (2020).

[41] B. Huang, G. Clark, E. Navarro-Moratalla, D. R. Klein, R. Cheng, K. L. Seyler, D. Zhong, E. Schmidgall, M. A. McGuire, D. H. Cobden, W. Yao, D. Xiao, P. Jarillo-Herrero, and X. Xu, Nature (London) **546**, 270 (2017).

[42] P. Jiang, C. Wang, D. Chen, Z. Zhong, Z. Yuan, Z.-Y. Lu, and W. Ji, Phys. Rev. B **99**, 144401 (2019).

[43] A. M. Leon, J. W. Gonzalez, J. Mejia-Lopez, F. C. de Lima, and E. S. Morell, 2D Mater. **7**, 035008 (2020).

[44] B. Zhai, J. Du, C. Shen, T. Wang, Y. Peng, Q. Zhang, and C. Xia, Phys. Rev. B **100**, 195307 (2019).

[45] I. Cucchi, A. Marrazzo, E. Cappelli, S. Ricco, F. Y. Bruno, S. Lisi, M. Hoesch, T. K. Kim, C. Cacho, C. Besnard, E. Giannini, N. Marzari, M. Gibertini, F. Baumberger, and A. Tamai, Phys. Rev. Lett. **124**, 106402 (2020).

[46] K. Kandrai, P. Vancso, G. Kukucska, J. Koltai, G. Baranka, A. Hoffmann, A. Pekker, K. Kamaras, Z. E. Horvath, A. Vymazalova, L. Tapaszto, and P. Nemes-Incze, Nano Lett. **20**, 5207 (2020).

[47] A. Marrazzo, M. Gibertini, D. Campi, N. Mounet, and N. Marzari, Phys. Rev. Lett. **120**, 117701 (2018).

[48] A. Marrazzo, M. Gibertini, D. Campi, N. Mounet, and N. Marzari, Nano Lett. **19**, 8431 (2019).

[49] A. Marrazzo, N. Marzari, and M. Gibertini, Phys. Rev. Res. **2**, 012063(R) (2020).

[50] See Supplemental Material at http://link.aps.org/supplemental/10.1103/PhysRevB.104.L121403 for the computational methods, configurations, and band structures of different stacking orders, electronic properties of h-BN/Pt$_2$HgSe$_3$/h-BN/CrI$_3$ and Pt$_2$HgSe$_3$/MnI$_2$ heterostructures, and the fitting parameters from first-principles results, which includes Refs. [35,43,47,56,62,65–72].

[51] D. Xiao, M.-C. Chang, and Q. Niu, Rev. Mod. Phys. **82**, 1959 (2010).

[52] J. Shi, G. Vignale, D. Xiao, and Q. Niu, Phys. Rev. Lett. **99**, 197202 (2007).

[53] W. Feng, G.-Y. Guo, J. Zhou, Y. Yao, and Q. Niu, Phys. Rev. B **92**, 144426 (2015).

[54] Y. Gao, S. A. Yang, and Q. Niu, Phys. Rev. B **91**, 214405 (2015).

[55] H. Zhou, C. Xiao, and Q. Niu, Phys. Rev. B **100**, 041406(R) (2019).

[56] A. A. Mostofi, J. R. Yates, Y. S. Lee, I. Souza, D. Vanderbilt, and N. Marzari, Comput. Phys. Commun. **178**, 685 (2008).

[57] M. P. L. Sancho, J. M. L. Sancho, and J. Rubio, J. Phys. F **14**, 1205 (1984).

[58] Q. Wu, S. Zhang, H. Song, M. Troyer, and A. A. Soluyanov, Comput. Phys. Commun. **224**, 405 (2018).

[59] Y. S. Hou, J. Kim, and R. Q. Wu, Sci. Adv. **5**, eaaw1874 (2019).

[60] Y. Uchiyama, A. Kutana, K. Watanabe, T. Taniguchi, K. Kojima, T. Endo, Y. Miyata, H. Shinohara, and R. Kitaura, npj 2D Mater. Appl. **3**, 26 (2019).

[61] X. Han, J. Lin, J. Liu, N. Wang, and D. Pan, J. Phys. Chem. C **123**, 14797 (2019).

[62] L. Rademaker and M. Gibertini, Phys. Rev. Mater **5**, 044201 (2021).

[63] F. Crasto de Lima, R. H. Miwa, and A. Fazzio, Phys. Rev. B **102**, 235153 (2020).

[64] C. Ma, H. Forster, and G. Grundmann, Crystals **10**, 687 (2020).

[65] P. E. Blochl, Phys. Rev. B **50**, 17953 (1994).

[66] G. Kresse and J. Furthmuller, Phys. Rev. B **54**, 11169 (1996).

[67] J. P. Perdew, J. A. Chevary, S. H. Vosko, K. A. Jackson, M. R. Pederson, D. J. Singh, and C. Fiolhais, Phys. Rev. B **46**, 6671 (1992).

[68] S. Qi, Z. Qiao, X. Deng, E. D. Cubuk, H. Chen, W. Zhu, E. Kaxiras, S. B. Zhang, X. Xu, and Z. Zhang, Phys. Rev. Lett. **117**, 056804 (2016).

[69] S. Grimme, J. Comput. Chem. **27**, 1787 (2006).

[70] L. Webster and J. Yan, Phys. Rev. B **98**, 144411 (2018).

[71] Y. Zhu, X. Kong, T. D. Rhone, and H. Guo, Phys. Rev. Mater. **2**, 081001 (2018).

[72] See www.fiz-karlsruhe.de.